Atmos. Chem. Phys. Discuss., 8, 19201–19247, 2008
www.atmos-chem-phys-discuss.net/8/19201/2008/

Atmospheric Chemistry and Physics Discussions

This discussion paper is/has been under review for the journal *Atmospheric Chemistry and Physics (ACP)*. Please refer to the corresponding final paper in *ACP* if available.

Identifying convective transport of carbon monoxide by comparing remotely sensed observations from TES with cloud modeling simulations

J. J. Halland[1], H. E. Fuelberg[1], K. E. Pickering[2], and M. Luo[3]

[1]Department of Meteorology, Florida State University, Tallahassee, Florida USA
[2]NASA Goddard Space Flight Center, Greenbelt, Maryland USA
[3]Jet Propulsion Laboratory, Pasadena, California USA

Received: 18 September 2008 – Accepted: 18 September 2008
– Published: 14 November 2008

Correspondence to: H. E. Fuelberg (fuelberg@met.fsu.edu)

Published by Copernicus Publications on behalf of the European Geosciences Union.

Abstract

Understanding the mechanisms that transport pollutants from the surface to the free atmosphere is important for determining the atmosphere's chemical composition. This study quantifies the vertical transport of tropospheric carbon monoxide (CO) by deep mesoscale convective systems and assesses the ability of the satellite-borne Tropospheric Emission Spectrometer (TES) to detect the resulting enhanced CO in the upper atmosphere. A squall line that is similar to one occurring during NASA's INTEX-B mission is simulated using a typical environmental wind shear profile and the 2-D Goddard Cumulus Ensemble model. The simulation provides post-convection CO profiles. The structure of the simulated squall line is examined, and its vertical transport of CO is quantified. Then, TES' ability to resolve the convectively modified CO distribution is documented using a "clear-sky" retrieval scheme. Results show that the simulated squall line transports the greatest mass of CO in the upper levels, with a value of 96 t upward and 67 t downward at 300 hPa. Maximum updraft speed is found to be unimportant in determining the net CO flux transported by a storm, but is important in determining the altitude to which the storm transports the boundary layer CO. Results indicate that TES has sufficient sensitivity to resolve convectively lofted CO, as long as the retrieval scene is cloud-free. TES swaths located immediately downwind of squall lines have the greatest chance of sensing convective transport because the impact of clouds on retrieval quality becomes less. A note of caution is to always analyze TES-derived CO data (or data from any satellite sensor) together with the retrieval averaging kernel diagonals or other parameters describing the information content of the retrieval.

1 Introduction

Anthropogenic pollution impacts many of the Earth's natural processes. Carbon monoxide (CO) is a byproduct of the incomplete combustion of carbon fuels (Jacob,

ACPD

8, 19201–19247, 2008

1999). With a lifetime of approximately one month, CO is an excellent tracer of pollution sources and pathways. CO also is a precursor to tropospheric ozone (O_3). CO concentrations near the surface in the United States typically are >200 ppbv in urban areas, 100–200 ppbv in rural areas, and <100 ppbv in remote areas (e.g., Jacob, 1999).

In the presence of nitrogen oxides (NO_x) and water vapor, the photochemical oxidation of CO produces tropospheric O_3 (Beer, 2006). O_3 then can create hydroxyl radicals (OH) by photolysis in the presence of water vapor, and OH is a major oxidant that removes pollutants such as methane and CO. Boundary layer pollutants that are rapidly transported to the free troposphere (FT) have increased lifetimes due to diminished loss mechanisms such as dry deposition, wet-scavenging by precipitation, and OH radicals (Park et al., 2001). In the upper troposphere where O_3 acts as a greenhouse gas, enhanced O_3 production in regions downwind of convection (Chatfield and Delany, 1990; Pickering et al., 1990; Park et al., 2001), along with the longer lifetimes of O_3 and its precursors, directly influence the Earth's radiation balance. Thus, identifying the concentrations and distributions of CO at different altitudes is vital to effectively calculating O_3 production and making better forecasts of the evolving radiation balance using climate models.

Pollutants generated at the surface can be transported vertically over depths ranging from tens to thousands of meters. The key factor determining the height of vertical transport is the type of meteorological system that is responsible. These systems range from synoptic scale cyclones, to mesoscale convective systems (MCS), to dry-convection and turbulence (Dickerson et al., 2007). Deep convection is one of the most efficient transporters of boundary layer air to the FT (Park et al., 2001; Dickerson et al., 2007). It is estimated that the mass of the ABL is vented ~90 times annually by clouds and cloud systems (Cotton et al., 1995). Calculations for the central United States suggest that nearly fifty-percent of ABL CO is transported to the FT by deep convection during summer (Thompson et al., 1994). Thus, estimating vertical transport by sub-grid scale mechanisms in chemical transport models is crucial for representing distributions of CO, O_3, and other species.

ACPD
8, 19201–19247, 2008

This study investigates the vertical transport of CO by mesoscale convective systems (MCSs). An MCS is a region of multi-cellular convection with a contiguous area of precipitation that spans 100 km or more in at least one horizontal direction (Glickman, 2000). The squall line is one prominent type of MCS, identified by its larger length-to-width ratio. We investigate a typical squall line in this study. Squall lines depend on environmental vertical wind shear to balance the horizontal vorticity generated by the convection's buoyant updraft, its rear-inflow jet (RIJ), and cold-pool at the surface (Rotunno et al., 1987; Weisman et al., 1988; Weisman and Rotunno, 2004). Dominant features of a squall line (Fig. 1) are its strong updraft and the ascending front-to-rear inflow that begins near the surface. Their magnitudes control how deep the convection can penetrate, and thus to what altitude surface pollutants are transported. Although a typical single-cell thunderstorm produces a maximum updraft of 8 to 15 $m\,s^{-1}$, deep multi-cellular convection often generates updrafts greater than 35 $m\,s^{-1}$ (Cotton et al., 1995). Pollutants transported in the convective updraft then can disperse from the cloud by detrainment along the core-updraft, the cloud anvil, and the edges of the cloud (Thompson et al., 1997). As a result, the ascending polluted air becomes diluted as it exits the cloud.

The 1985 PRESTORM project provided some of the first direct measurements in the anvils of convective storms. Dickerson et al. (1987) found that the anvil contained 64% ABL air and 36% upper tropospheric air after including the effects of entrainment. Pickering et al. (1989) identified enhanced layers of CO due to cumulonimbus venting over 500 km upwind. Pickering et al. (1990) related significant O_3 enhancements to convective injection of precursors into the upper troposphere (UT). Their research identified a major source of UT pollution that then can be rapidly transported horizontally to other regions.

Recent field projects also have examined mechanisms producing long-range chemical transport (Dickerson et al., 2007; Singh et al., 2006, 2007). A comparison of transport processes in northeast China and the northeast United States found that different mechanisms were involved (Dickerson et al., 2007). Dry convection was the promi-

ACPD
8, 19201–19247, 2008

nent pollution transporter over China during the spring season. However in the United States, deep, moist convection was the dominant transporter. Although both types of convection vented PBL air to the FT, the lack of wet-deposition in dry convection was speculated to be the main cause of enhanced pollution-venting over China (Dickerson et al., 2007).

The boundary layer venting of pollution by both fair-weather cumulus and deep convection has been successfully modeled for over two decades (Niewiadomski, 1986; Tremblay and Leighton, 1986; Pickering et al., 1995). Simulations of towering cumulus (Niewiadomski, 1986) revealed pollutant reduction percentages and vertical transport ratios (volume of sub-cloud air transported through the cloud base relative to the total volume of air below the cloud layer) of 15 and 23 percent, respectively. These values are similar to those found previously for cumulus outflow (Isaac et al., 1983). In a study of O_3 production downstream of deep convection over Brazil, nearly all of the air parcels in the anvil originated in the boundary layer (Thompson et al., 1997). Based on back trajectories, Thompson et al. found that many parcels were transported from 0.3 km to 15 km AGL in less than 30 min. The vertical transport of CO by warm-conveyor belts (WCB) in middle latitude cyclones was studied by Kiley and Fuelberg (2006). They found that the dominant vertical forcing mechanism was the Laplacian of latent heat release which is large in areas of deep convection. Deep convection in weak synoptic cyclones proved especially critical for the development of WCB-like transport. Other studies that have modeled or directly sampled pollution transport by both synoptic and mesoscale weather systems include Pickering et al. (1989), Park et al. (2001), Hannan et al. (2003), and Dickerson et al. (2007).

Since vertical transport occurs on a global scale, satellite remote sensing is the only way that it can be documented. NASA launched the Tropospheric Emission Spectrometer (TES) instrument onboard the Aura platform in 2004. TES utilizes a completely different technology than previous CO remote sensors, enabling it to make high-resolution retrievals of several atmospheric variables including temperature, water vapor, CO, and ozone. TES can make a global survey of all variables in approximately one day (Beer,

ACPD
8, 19201–19247, 2008

2006). We use TES derived CO profiles in this study, and additional details are given in Sect. 2.

Our first objective is to quantify the vertical transport of lower tropospheric air by a squall line. The squall line is simulated using the 2-D Goddard Cumulus Ensemble (GCE) model which provides post-convection CO profiles. Comparisons with pre-convective profiles describe the vertical transport. The second objective is to gain insight into TES' ability to detect CO convective transport. This is achieved by inputting the pre- and post-convection simulated CO profiles to the TES retrieval algorithm to obtain synthetic retrievals.

2 Data and methodology

2.1 TES Instrument and CO profile retrievals

The Tropospheric Emission Spectrometer (TES) is housed on the Earth Observing System Aura platform (Beer, 2006). Aura's orbit is near-polar, sun-synchronous at an altitude of 705 km, with an ascending equatorial crossing near 13:35 local solar time. TES is a nadir viewing infrared Fourier transform spectrometer that samples the atmospheric absorption/emission spectra of several gases (Beer, 2006; Bowman, 2006). TES functions in two primary observation modes, the global survey mode (GS) and the step and stare mode (SS). The GS mode consists of 16 orbits with a successive nadir sampling distance of 182 km along the track, while the SS mode spans 45 degrees latitude and consists of 150 nadir observations at a separation of 40 km along the track over 5×8 km horizontal footprints. TES' high spectral resolution of 0.1 cm^{-1} (nadir viewing) enables it to provide vertical CO profiles in the troposphere with 1–2 degrees of freedom for signal (DOF) in the tropics to mid latitude regions (Luo et al., 2007).

The TES retrieval algorithm is an optimal estimation method that minimizes the residual between the observed and modeled radiances (Rodgers, 2003; Bowman et al., 2006). The a priori constraints represented by the atmospheric species profiles

ACPD
8, 19201–19247, 2008

and their uncertainties are explicitly applied. Unlike cloud-clearing and cloud-masking schemes adopted by other satellite instruments, TES' cloud retrieval strategy assumes a layer of effective cloud with the spectral dependent extinctions and the layer pressure retrieved (Kulawik et al., 2006). In addition to these effective cloud data provided in the data files, averaging kernels for the profile retrievals also are provided.

The averaging kernels and the a priori profiles provide useful information on understanding the retrieved species profiles. A retrieved profile is not the true atmospheric profile at a given location and time. The following equation approximates the relationship between the true profile, x_t^i, the a priori profile, $x_{t,\mathrm{TES}}^i$, and the retrieved profile (Rodgers, 2003; Luo et al., 2007),

$$\hat{x}_t^i = x_{t,\mathrm{TES}}^i + A_t^i(x_t^i - x_{t,\mathrm{TES}}^i) + \varepsilon_t^i \quad , \tag{1}$$

where A_t^i is the averaging kernel matrix for the profile and ε_t^i is the observational error due to instrument noise. In the ideal case, when the averaging kernel is a unit matrix, the retrieved profile equals the true profile. However, the remote sensing solutions are far from the ideal case, due to the lack of information in the observed spectral radiances about the species profiles and the limitations of the instrument characteristics and performances. We will show examples of the TES averaging kernel for CO retrievals in later sections. In the worst case, there is no information on atmospheric CO profiles from the nadir spectral measurements (very small averaging kernel values). The retrieved profile then is dominated by the a priori profile. An example of this case is a cloud. The TES observed spectra contain no information on the CO distribution within and below clouds. The averaging kernels in this vertical portion are very small and the retrieved CO values are dominated by the a priori profile.

2.2 Creating synthetic CO profiles

Using (1), TES a priori and averaging kernel data on 13 March 2006 during the INTEX-B campaign at 39° N were used to generate two sets of synthetic TES retrieved CO profiles. The first set of synthetic profiles used CO data from the GEOS-Chem chemical

ACPD
8, 19201–19247, 2008

transport model (CTM, Bey et al., 2001) as the true state profile prior to convective activity. The second set of retrievals, the post-convection true state profiles, was based on CO data output from the 2-D Goddard Cumulus Ensemble (GCE) cloud model (Tao and Simpson, 1993). Specifically, the GCE output was considered the true state of the atmosphere after CO had been lofted by a storm system. Details of the GCE and GEOS-Chem model are given in Sects. 2.3 and 2.4, respectively.

The model-derived CO profiles were interpolated vertically to the TES pressure levels. Since the top of the model domain (troposphere) did not extend to the altitude at which TES makes retrievals, all pressure levels above the top of the model domain contain the TES retrievals as the true state values (Luo and Worden, 2007). Equation (1) then is used to generate the synthetic TES CO retrieval profiles. Comparisons between these simulated satellite retrieved profiles and the model true profiles enable us to determine how well TES depicts the convective lofting of CO.

2.3 Cloud-model

The 2-D Goddard Cumulus Ensemble (GCE) (Tao and Simpson, 1993; Tao et al., 2003) is a convective cloud-resolving model that has been used to understand cloud interactions with each other, with the surrounding environment, and with trace gas distributions (Soong and Tao, 1980; Tao and Simpson, 1984; Scala et al., 1990; Pickering et al., 1991, 1992a, b, c). Its governing equations are non-hydrostatic since the horizontal and vertical scales of convection are similar. The model explicitly resolves gravity waves generated by the developing cloud in the x-z plane (Tao and Simpson, 1993) and contains microphysical processes that are sophisticated and sensitive to the dynamic processes resolved (Tao et al., 1991; Tao and Simpson, 1993), including the complete microphysics for all water phases (Soong and Ogura, 1980; Soong and Tao, 1980; Tao and Soong, 1986). An on-line chemical tracer advection capability has been added to the 2-D GCE model by Stenchikov et al. (1996).

The horizontal grid of the 2-D GCE consists of 514 points spanning 470 km, with 33 vertical levels on a stretched grid whose spacing ranges from 220 m near the surface

ACPD
8, 19201–19247, 2008

to 1050 m at the top of the 25 km vertical domain. The model has open-type lateral boundary conditions, free-slip boundary conditions for model variables, and a 5 km Rayleigh relaxation (absorbing) layer at its top (Klemp and Wilhelmson, 1978; Tao and Simpson, 1993). All of our simulations used the model parameter settings listed in Table 1. A full description, including model equations and specific sensitivity studies, is provided in Tao and Simpson (1993) and Tao et al. (2003).

2.4 Meteorological and chemical data

Background CO describing the environment prior to convection was obtained from the 3-D GEOS-Chem global chemical transport model (Bey et al., 2001). Its input emissions for countries with regulated emissions, like the US, were derived from quarter-degree hourly inventories of anthropogenic and biomass burning sources distributed by the Environmental Protection Agency (EPA) and National Emissions Inventory (NEI) for 1999 (GEOS-Chem User's Guide, 2005). In non-regulated countries, model emissions were based on global base emission inventories from Wang et al. (1998) and CO emissions developed at Harvard University. Values were scaled to the present year based on carbon dioxide (CO_2) emissions from liquid fuels (Bey et al., 2001). The emissions data include both weekday and weekend rates, which for GEOS-Chem processing are combined into one-degree monthly bins.

GEOS-Chem version 7-04-09 uses assimilated meteorological fields from the Goddard Earth Observing System-Version 4 (GEOS-4) with a native resolution of $1^\circ \times 1.25^\circ$ (latitude×longitude) grid and 55 vertical levels (Bloom et al., 2005), processed on a $2^\circ \times 2.5^\circ$ grid with a reduced vertical spacing of 30 levels in a hybrid sigma-pressure coordinate system. Deep convection and shallow convection are parameterized separately in GEOS-4, following schemes described in Zhang and McFarlane (1995) and Hack (1994).

ACPD
8, 19201–19247, 2008

2.5 Squall line simulations

Mid-latitude squall lines have been simulated using two-dimensional cloud resolving models for over two decades (e.g., Ogura and Liou, 1980; Thorpe et al., 1982; Fovell and Ogura, 1988; Rotunno et al., 1987; Pickering et al., 1995). A 2-D model is justified since a squall line's structure varies mostly in the line normal direction (Fovell and Ogura, 1988) and since wind shear perpendicular to the line is what yields a steady convective cell (Rotunno et al., 1988).

The thermodynamic sounding used for our GCE integrations (Fig. 2) has been employed in previous modeling studies of mid-latitude squall lines (Weisman and Klemp, 1982, 1984; Rotunno et al., 1988; Lericos et al., 2006) and was derived from soundings of typical squall line environments (Ogura and Liou, 1980; Bluestein and Jain, 1985; Fovell and Ogura, 1988). The pre-squall line thermodynamic environment over the US central plains on 13 March 2006 during NASA's INTEX-B field project (Singh et al. 2008) was similar to the sounding in Fig. 2. Therefore, our pre-convective CO sounding was taken from the GEOS-Chem model near 41.61° N, 90.58° W at 00:00 UTC 13 March 2006 (Fig. 3). The GEOS-4 300 hPa cloud mass-flux field (not-shown) confirmed that no convection was located in the area at this time. Therefore, the CO profile represents nearly undisturbed background values prior to the arrival of the squall line. The CO profile was interpolated to 20 vertical levels and used as background values in the GCE simulations. The grid spacing for the CO tracer (not the same as GCE resolution) consisted of 500 m layers between the surface and 2500 m and then 1 km layers to 17.5 km with the concentration at 17.5 km used until the top of the model. CO profiles then were made from the GEOS-Chem output at each TES footprint as discussed in Sect. 2.6.

Low-level environmental wind shear is crucial for the development of steady convection (Thorpe et al., 1982; Fovell and Ogura, 1988; Rotunno et al., 1988; Lericos et al., 2006). Many previous squall line simulations have used shear-layer depths between 2.5 and 5.0 km, with vertical wind shears ranging from 7 to 25 m s^{-1}, respectively. Most

ACPD
8, 19201–19247, 2008

then maintained uniform winds above the shear layer, with the exception of Thorpe et al. (1982). We tested several shear profiles that were adapted from those of Fovell and Ogura (1988) and Lericos et al. (2006). The profile in Fig. 4 most resembled conditions in our pre-storm environment since it contains a weak jet near 9 km. The strongest shear of 17.5 m s^{-1} is between 350 m and 2450 m, which gradually weakens to produce a peak wind speed of 12.5 m s^{-1} at 8950 m. The shear then becomes negative, linearly decreasing 2.5 m s^{-1} between 8950 m and 20 650 m, the top of the sounding. The vertical transport of CO due to the squall line resulting from this wind profile is presented in later sections

2.6 TES retrievals

We assumed that the GEOS-Chem CO profile used in our GCE simulations was the true atmospheric state of the pre-convective environment (Sect. 2.4). CO retrievals were calculated at every horizontal grid point in the GCE model domain to determine how TES would depict the "pre-convection" CO concentrations. Then we took the GCE CO profiles representing 'post-convection' concentrations and performed the same retrieval calculations at every grid point. We used the averaging kernel from the clear-sky retrieval of profile 17 from the TES swath (RUNID 3443) on 13 March 2006 and GEOS-Chem derived a priori background CO as the clear pre-squall line CO profile.

3 Results

3.1 Squall line structure

We first establish the close agreement between our squall line simulation and those of previous studies who used similar wind shear profiles. A time-series of maximum/minimum storm vertical motion is shown in Fig. 5, while a time-series of maximum reflectivity is in Fig. 6. The plots of reflectivity were computed over a 1.5 degree longitude (130 km at 39° N) subset of our total computational domain.

ACPD
8, 19201–19247, 2008

The storm first evolves through an "initial phase" in which the simulated cold pool initiates the convection (Fig. 5) (Rotunno et al., 1988). This initial phase is similar to Fig. 17 of Fovell and Ogura (1988). The magnitude of our initial updrafts is ~18 m s^{-1} at ~30 min into the simulation, before abruptly decreasing to ~5 m s^{-1} at ~60 min. This marks the collapse of the initial cell, and the initiation of weak convection to the west (left) and east (right) (Fig. 7). Downdrafts from each cell then begin to intensify, leading to the formation of a single convective cell near 110 min. The storm then evolves into a vigorous series of pulsating updrafts and downdrafts (Fig. 5). The storm's cyclic pattern of intensification and weakening corresponds to the initiation of new cells in the line and the decay of old cells (Fig. 8). Specifically, the cold pool due to the storm's downdraft surges rearward (to the left) where it forces new convection (Figs. 7 and 8) within a few kilometers of the main reflectivity core.

The reflectivity patterns in Fig. 8 reveal a prominent forward anvil. And, the relatively strong westerly winds in the mid-levels tend to flow toward the surface as they approach the cell (Figs. 8 and 9), corresponding to the rear inflow jet in Fig. 1. We determined cloud top heights by summing the individual hydrometeors into a total hydrometeor field, using the value 0.01 g kg^{-1} as the threshold for the outer cloud edge. The cloud tops initially are below 10 km, but after storm intensification near 210 min, they consistently extend above ~12 km (Fig. 8). Updrafts range from 5 to 27 m s^{-1}, while downdrafts vary between 4 and 14 m s^{-1}. The variability of our maximum updrafts appears to be several meters per second greater than found by Fovell and Ogura (1988, Fig. 16). A possible reason is the time step at which the data are plotted. Our data are output at 1 min intervals for 8 h, while those in Fovell and Ogura appear to be at 5 min intervals for a 12 h simulation. This factor alone produces greater variation in our results.

To summarize, the reflectivity patterns and maximum updrafts of our simulated squall line are consistent with those of previous simulations using similar ambient shear profiles (e.g., Fovell and Ogura, 1988). The storm contained strong vertical velocities that underwent cyclic evolutions as new cells developed and decayed. The storm had

ACPD
8, 19201–19247, 2008

a dominant forward anvil, a base reflectivity region varying between 10 and 40 km in width, and weak near-surface reflectivity located east (right) of the storm (Fig. 9). Based on these similarities with previous studies, we use the simulation to investigate CO transport by deep convection.

3.2 CO transport characteristics

We next describe the vertical distribution and mass flux of CO produced by the simulated squall line. Once the convection begins (~40 min, not shown), boundary layer CO is injected into the FT by the storm's strong updrafts. By 180 min (Fig. 10a), CO penetrates the stable region of the tropopause, with the lofted CO dispersed predominately eastward (toward the right) in the upper levels. As the CO reaches the tropopause, it begins to dilute as weaker concentrations of ambient CO are mixed into it.

The CO concentration of the dry mid-level air descending on the upshear (left) side of the storm (Fig. 8) is smaller than at the surface. This air entering from the rear enhances the storm's downdraft and the mass of the cold pool, a feature also seen in previous studies (Ogura and Liou, 1980; Thorpe et al., 1982). This causes the cold pool to spread eastward where it enhances the existing convection, and westward where new convection is initiated. The westward spread of the cold pool reduces CO in the boundary layer of the storm's wake (Fig. 10a–c).

The lofted CO is carried downwind by the relatively strong upper level winds centered near 9 km (Fig. 10). The downdrafts carrying upper level air back to the surface contain less CO than if the upper level winds had been near zero and the lofted CO had remained near the region of the incipient downdrafts. By the end of the simulation (480 min), the CO plume aloft has developed a well defined forward component (Fig. 10c). Near the base of the updraft (i.e., near the surface) (Fig. 10b), there is a demarcation between the downdraft air and the air ahead of the storm . This may be a result of downdrafts occurring in brief intense bursts. This variability in downdraft intensity may cause different levels of mixing near the surface, a possible mechanism for the CO signature in the wake of the storm. As is well known, the length of time that

ACPD
8, 19201–19247, 2008

the relatively clean downdraft air influences an area, the larger is the CO anomaly.

We calculated a time series of CO mass flux at 850, 500, and 300 hPa using the equation (Dickerson, 2005)

$$\text{Mass} = (\text{MC} \cdot w) \cdot \text{Area} \cdot \text{Time}, \quad (2)$$

where mass is the total amount of CO transported per time increment, MC is the mass concentration of CO (g m^{-3}), w is the vertical velocity (m s^{-1}), and the time period is 10 min (600 s). The mass concentration MC is derived from the volume mixing ratio (VMR) in parts per billion, the standard output from the GCE, using the ideal gas law

$$\text{MC}\left(\text{g/m}^3\right) = \frac{P_{\text{LEV}}\text{MW}_{\text{CO}}}{R \cdot T} \cdot \frac{1000 \cdot \text{liters}}{\text{m}^3} \cdot \frac{\text{ppbv}}{10^9} \quad (3)$$

where P_{LEV} is the pressure level of the mass flux calculation, MW_{CO} is the molecular weight of CO (g/g-mol), R is the universal gas constant (0.08206 (l-atm)/(g-mol-K)), T is temperature (K), and ppbv is the CO concentration in parts per billion. The area for the flux calculation was the grid cell width multiplied by 1 km. If the vertical velocity at a level was negative, the concentration above that level was used for the calculation. Conversely if the vertical velocity at the level was positive, the concentration below the level was used.

Time series of CO vertical flux at 300, 500, and 850 hPa are given in Fig. 11, while values for the three levels are given in Table 2. One should note the persistent quasi-balance between the upward and downward mass fluxes (Fig. 11). Because the maximum updraft speed at any time step is approximately twice that of the downdraft (Fig. 5a), one might expect that the downward flux would be smaller than the upward flux. However, this is not observed, likely because of the different overall sizes of the updraft and downdraft regions. Thus, the maximum updraft and downdraft velocity help identify the height to which surface CO can be lofted, but not the quantity of CO that is transported. The storm maintains a clockwise circulation east of the main updraft which continually circulates CO away from and toward the surface. We believe that

ACPD
8, 19201–19247, 2008

these circulations lead to the enhancement of the upward and downward CO mass flux at 500 hPa (Table 2).

The values of "Net Mass Flux" in Table 2 can be misleading because they are the sum of the upward and downward mass flux at each level. That is, they do not quantify the CO actually transported away from the surface. For example, the convective transport of CO out of the boundary layer (below 850 hPa) is 33.0 metric tons over the 8 h simulation. However, there is net 850 hPa CO flux toward the surface (–12.6 metric tons). This difference likely is the result of the core updraft developing above the 850 hPa level. Thus, because the downdrafts transport CO to the surface, they consistently cross the 850 hPa level. It is important to note that the concentration of CO in the downdraft typically is smaller than in the updraft, as seen in the wake of the storm (Fig. 10). Therefore, the greater downward mass flux could be a result of circulations ahead of the main updraft transporting greater CO concentrations toward the surface. Therefore, decreases in boundary layer CO are due to a combination of upward venting and the downward transport of cleaner air.

The change in CO concentration between storm initiation and the end of the simulation (Fig. 12) summarizes our findings regarding convective transport. The squall line's strong updrafts lead to large CO increases in the middle and upper troposphere. The ambient winds carry the enhanced CO downwind of the convection. Upwind of the storm, the rear inflow jet and downdrafts lead to decreases in CO, particularly in the low levels.

Although our simulations were performed using a 2-D model, actual convective transport occurs in three dimensions. It is informative to estimate the amount of CO that is transported by a 3-dimensional squall line of the type described here. We will assume that our initial CO concentrations (Fig. 3) are uniform along the squall line and that the line is broken, consisting of storms of 30 km (N-S) in size, separated by 15 km, and extending for 450 km in length. These assumptions produce a transport of 9.9×10^3 metric tons of CO out of the boundary layer over the 8 h simulation period, 3.89×10^4 metric tons past 500 hPa, and 2.88×10^4 metric tons of CO above 300 hPa over the 8 h sim-

ACPD
8, 19201–19247, 2008

ulation. Thus, as noted in previous studies (e.g., Cotton et al., 1995; Dickerson et al., 1987), convection truly is a powerful transport mechanism of CO. How well the TES instrument resolves these CO enhancements is discussed in the next section.

3.3 Synthetic CO retrievals

A major goal of this study is to identify how well the TES instrument resolves the vertical transport of CO by deep convection. As described earlier, the 2-D GCE model was used to generate atmospheric CO concentrations during the life of a simulated squall line. Then, by using a clear sky averaging kernel, we retrieved the synthetic CO concentrations that TES would have seen if it had scanned the region before, during, and after the convection–assuming "transparent clouds". This section presents CO results for the squall line simulation described previously, along with an example of how well TES viewed an actual squall line having similar characteristics.

We first examine how TES resolved the CO distribution in the pre-squall line environment. The initial CO profile used in the GCE was taken from GEOS-Chem (Fig. 3) and was used at all horizontal grid points in the model domain. The profile was located in a cloud-free region of the pre-squall line environment at 41.61° N, 90.58° W at 00:00 UTC 13 March 2006 during the INTEX-B mission (Singh et al., 2008). By 08:15 UTC 13 March (Fig. 13) a well developed squall line stretched through this area. We chose the averaging kernel profile at a cloud-free location (from scan 17 of the Level 2 TES file for RUNID 3443 on 13 March) for our synthetic retrieval locations because its pre-storm thermodynamic environment was similar to that in our GCE model run. Using the same averaging kernel profile at every location means that atmospheric thermodynamics will not be a factor in causing retrieval differences (Luo et al., 2007).

A brief explanation of the averaging kernel is useful at this time. The diagonal of the averaging kernel describes the fractional contribution of the true concentration of the species at the pressure level, relative to the sum of all elements of the averaging kernel. The magnitude of the averaging kernel diagonal depends on the number of pressure levels that the satellite retrieves, and therefore is unique to the retrieval. A

ACPD
8, 19201–19247, 2008

TES CO averaging kernel diagonal containing the greatest information has a value of ~0.1 (S. Kulawik, personal communication, 2007). The diagonal profile values (Fig. 14) were available in the level 2 data product supplied by the TES science team (TES L2 Data User's Guide, 2006). The averaging kernel diagonal that we used for all points in the model domain only has values ~0.1 between 650 and 380 hPa. Therefore, this is the layer having the greatest sensitivity to our initial and convectively modified CO concentrations. Diagonal values decrease sharply below this layer and more gradually above, reaching values as small as ~0.01.

Magnitudes of the synthetic TES retrievals for the initial CO field (Fig. 15b) differ from those of the input GEOS-Chem data (Fig. 15a); however, patterns of the initial and retrieved fields are similar. Some of the greatest differences are located near the surface, where the TES- retrieved CO is ~30 ppb greater than the GEOS-Chem input. Concentrations in the middle troposphere are similar to the original, while TES values are somewhat greater than the initial values near 200 hPa. Slight differences between the thermodynamic profile in the original TES retrieval and the one used in the modeling are a possible explanation for differences in the background CO field by the synthetic TES retrieval. Since we used the same averaging kernel and a priori profile at every grid point, we can interpret the convectively altered profiles by considering this initial difference. These differences are important to remember as we describe the synthetic TES retrievals of the convectively altered CO field (hereafter CCO).

We next present results of the synthetic TES CO retrievals from the simulated squall line (Fig. 16). We have superimposed the storm's cloudy region over the domain (based on Fig. 10) to identify areas where clouds prevent the "clear-sky" retrievals from being reliable. Specifically, any region beneath the cloudy area would not be properly sensed by a TES instrument in actual orbit; however, all regions above the cloudy scene reflect the sensitivity of the "clear-sky" averaging kernel. Figure 16 shows synthetic TES retrievals for the GCE model domain at a) 180 min, b) 300 min, and c) 480 min into the simulated storm.

Comparing Figs. 10 and 16 reveals that TES resolves the general pattern of the

ACPD
8, 19201–19247, 2008

CCO field. The plume is detected at heights nearly identical to those from the GCE, even in the cloudy area since we assumed a "clear-sky" averaging kernel (Fig. 14). At 300 and 480 min (Fig. 16b–c) respectively, relatively small CO concentrations are located upwind (left) of the storm in the upper levels, but enhanced values are produced above the cloud. The synthetic TES retrievals also reveal the large concentrations of CO within the storm's updraft in this "clear-sky" situation. In the "real world" this region would be enshrouded by deep cumulonimbus clouds that would prevent TES from adequately sensing the area. However, due to the strong updraft-induced lofting of CO deep into the troposphere and lower stratosphere where environmental winds are relatively strong, much of the lofted CO will be transported above the storm and downwind of the cloudy region. Thus, CO enhancements sensed above deep convection likely signify even larger CO enhancements below that level when the shape of the averaging kernel profile is similar to the one applied in our retrievals.

This hypothesis is explored further using Fig. 17 which shows differences (ppbv) between the initial synthetic TES retrievals and those of the CCO field. The increased CO above the storm system can be explained by the structure of the averaging kernels, best shown by its diagonal. The averaging kernel in our case obtains most of its information about the atmosphere's true state (GCE output) in the middle levels (Fig. 14). And, this is the layer where greatest CO concentrations are located (Fig. 10). The large values retrieved in the middle levels influence the TES retrievals above and below the layer to which TES is most sensitive. Thus, CCO enhancements within and above the storm are too great, since the GCE produced smaller CO increases. Thus in the "real world", the interpretation of TES data must consider the averaging kernel diagonal in the area of study. That sensitivity information enables one to speculate about the concentration in the lower and middle troposphere based on enhanced CO in the upper levels of the retrieval.

A somewhat surprising feature in Fig. 17 is the reduction in detected CO concentrations near the surface in the wake (left) of the storm system. Although the magnitude of this reduction is ~15 ppbv (compared with ~30 ppbv from the GCE model) (Figs. 10c

ACPD
8, 19201–19247, 2008

and 17c), the general area of diminished CO is correctly depicted.

MCSs by definition are associated with deep clouds that usually spread out ahead of and behind the storm system in the upper levels. These clouds are the major reason why the averaging kernel diagonal is not ~0.1 but much smaller, i.e., the clouds are not handled adequately by the TES retrieval algorithm. Fortunately, however, steering winds in the upper levels of the MCS environment typically are strong enough to carry lofted pollution away from the cloudy region. Therefore, the best way to infer lofted pollution using the TES instrument is to look downwind of the system after the storm has been organized for several hours.

3.4 Observed TES CO retrievals

As a final point, we investigate actual TES retrievals for a squall line at 08:04 UTC 13 March 2006 during INTEX-B – the case whose CO profile and averaging kernel were used in the earlier simulations. The TES swath intersects the squall line over the Midwest (Fig. 18), and the locations of missing profiles are immediately apparent (Figs. 18 and 19). These profiles are skipped because the multiple cloud layers or deep convection caused the retrieval scheme to determine that there is insufficient scene information. Nonetheless, some of the profiles that were retained near the squall line exhibit very small values of the averaging kernel diagonal (Fig. 19b). Thus, they contain little information about the true atmospheric state. For example, retrievals 0 and 5 appear to show enhanced values throughout the vertical column (Fig. 19a). However, an examination of the averaging kernel diagonals for each profile (Fig. 19b) indicates that the enhancement actually is false because the diagonal values are near zero at all levels. Retrieval 7 is the first in the swath to include significant information about the true state of the atmosphere. Its kernel diagonal (Fig. 19b) has a peak of ~0.08 in the mid-troposphere, with an overall curve similar to that used in our synthetic TES retrievals (Fig. 14b). This profile also exhibits a vertical distribution of CO that is similar to the pattern found in the synthetic retrievals, indicating the effects of convective transport. Retrieval 7 is located ~60 km downwind of the leading edge of the squall line.

ACPD
8, 19201–19247, 2008

When analyzing profile 7, the reader is reminded that the TES algorithm enhances true CO concentrations near the surface as was seen in the synthetic profiles (Fig. 15). One also should note that GEOS-Chem produced surface CO values of ∼130 ppbv in this area, which is ∼40 ppbv less than the TES-retrieved concentration at this same location (not shown). Retrieval 10 also contains significant valid information, with the greatest portion coming from the upper levels of the atmosphere. This suggests that the convective impact may be minimal in this case. This retrieval is located farther downwind of the squall line than retrieval 7.

To summarize, we stress that TES retrievals by themselves can be misleading especially in regions of cumulonimbus clouds. However, knowledge of profile sensitivities at each level can lead to better understanding and use of TES retrievals in both the model domain and real atmosphere.

4 Conclusions

This study has quantified the vertical transport of lower tropospheric carbon monoxide (CO) by deep convection associated with mesoscale convective systems. Specifically, a squall line was simulated based on a typical environmental wind shear profile using the 2-D Goddard Cumulus Ensemble model. The wind profile had a varying shear of 17 m s^{-1} over a 9 km depth. The simulation provided post-convection CO profiles. The ability of the TES instrument to resolve the convectively modified CO distributions then was analyzed using a "clear-sky" retrieval methodology.

Results showed that the squall line transported a large mass of CO into the upper levels, specifically 96 t upward and 67 t downward at 300 hPa. Sensitivity tests revealed that although updraft speed was unimportant in determining the net CO flux transported by the storm, it was important in determining the altitude to which the storm transported boundary layer CO.

We conclude that TES is able to detect convectively transported CO as seen both in synthetic retrievals based on convective modeled output and from an actual convective

ACPD
8, 19201–19247, 2008

event. However, we stress that this can be accomplished only with the aid of the averaging kernel diagonals that are supplied with the Level 2 data files. The kernel diagonals describe the sensitivity of the CO retrieval at different pressure levels. TES swaths that are located immediately downwind of squall lines were found to have the greatest chance of detecting convective transport because the impact of clouds on retrieval quality becomes less of an issue. The stronger middle and upper level winds that are associated with intense convection will advect the CO downwind and beyond the cloudy area. CO enhancements above the storm's cloud tops were sensed by TES retrievals using CO profiles from a cloud model simulation as the true atmospheric state. However, since the major storm-induced CO enhancements occur in the upper levels, the retrieval algorithm tends to smear this enhancement above and below its altitude. Thus, a note of caution is to always analyze TES-derived CO data (or data from any satellite sensor) together with the retrieval averaging kernel diagonals or other parameters describing the information content of the retrieval. Although the retrieved values can be misleading, information about the sensitivity of the retrieval allows one to selectively use the data in analyses and studies of pollution transport.

Acknowledgements. We appreciate the helpful advice of Annmarie Eldering and Greg Osterman at JPL. We also thank Wei-Kuo Tao of NASA/GSFC for use of the GCE model. This research was sponsored by NASA's Tropospheric Chemistry Program under grant NNG06B43G to Florida State University.

References

Beer, R.: TES on the Aura Mission: Scientific Objectives, Measurements, and Analysis Overview, IEEE Trans. Geosci. Rem. Sens., 44, 1102–1105, 2006.

Bey, I., Aumont, B., and Toupance, G.: A modeling study of the nighttime radical chemistry in the lower continental troposphere: 1. Development of a detailed chemical mechanism including nighttime chemistry, J. Geophys. Res., 106, 9959–9990, 2001.

Bloom, S., da Silva, A., Dee, D., Bosilovich, M., Chern, J.-D., Pawson, S., Schubert, S., Sienkiewicz, M., Stajner, I., Tan, W.-W., and Wu, M.-L.: Documentation and Validation of

the Goddard Earth Observing System (GEOS) Data Assimilation System – Version 4, Technical Report Series on Global Modeling and Data Assimilation 104606, 26, 2005.
Bluestein, H. B. and Jain, M. H.: Formation of mesoscale lines of precipitation: Severe squall lines in Oklahoma during the spring, J.Atmos. Sci., 42, 1711–1732, 1985.
Bowman, K. W., Rodgers, C. D., Kulawik, S. S., Worden, J., Sarkissian, E., Osterman, G., Steck, T., Ming Lou, Eldering, A., Shephard, M., Worden, H., Lampel, M., Clough, S., Brown, P., Rinsland, C., Gunson, M., and Beer, R.: Tropospheric emission spectrometer: Retrieval method and error analysis, IEEE Trans. Geosci. Rem. Sens., 44, 1297–1307, 2006.
Chatfield, R. B. and Delany, A. C.: Convection links biomass burning to increased tropical ozone: However, models will tend to over predict O_3, J. Geophys. Res., 95, 18 473–18 488, 1990.
Cotton, W. R., Alexander, G. D., Hertenstein, R., Walko, R. L., McAnelly, R. L., and Nicholls, M.: Cloud venting-A review and some new global annual estimates, Earth-Sci. Rev., 39, 169–206, 1995.
Dickerson, R. R., Huffman, G. J., Luke, W. T., Nunnermacker, L. J., Pickering, K. E., Leslie, A. C. D., Lindsey, C. G., Slinn, W. G. N., Kelly, T. J., Daum, P. H., Delany, A. C., Greenberg, J. P., Zimmerman, P. R., Boatman, J. F., Ray, J. D., and Stedman, D. H.: Thunderstorms: An important mechanism in the transport of pollutants, Science, 237, 460–465, 1987.
Dickerson, R. R.: METO 434 Air Pollution, 26 January 2005, Dept. of Metr., U. of Maryland, http://www.atmos.umd.edu/~russ/434L2.ppt#256,1,LECTURE2, 2007.
Dickerson, R. R., Li, C., Li, Z., Marufu, L. T., Stehr, J. W., Chen, H., Wang, P., Xia, X., Ban, X., Gong, F., Yuan, J., and Yan, J.: Aircraft observations of dust and pollutants over N. E. China: Insight into the meteorological mechanisms of long range transport, J. Geophys. Res., 112, D24S90, doi:10.1029/2007JD008999, 2007.
Fovell, R. G. and Ogura, Y.: Numerical simulation of a midlatitude squall line in two dimensions, J. Atmos. Sci., 45, 3846–3879, 1988.
GEOS-Chem User's Guide. Vers. 7.03.06: 8 November 2005. Atmos. Chem. Modeling Group, Harvard University, http://www-as.harvard.edu/chemistry/trop/geos/doc/man/index.html, 2007.
Glickman, T. S.: Glossary of Meteorology, 2nd ed., Boston, Massachusetts: American Meteorological Society, 2000.
Hack, J J.: Parameterization of moist convection in the National Center for Atmospheric Research Community Climate Model (CCM2), J. Geophys. Res., 99, 5551–5568, 1994.

Hannan, J. R., Fuelberg, H. E., Crawford, J. H., Sachse, G. W., and Blake, D. R.: Role of wave cyclones in transporting boundary layer air to the free troposphere during the spring 2001 NASA/TRACE-P experiment, J. Geophys. Res., 108(D20), 8785, doi:10.1029/2002JD003105, 2003.

Isaac, G. A., Joe, P. I., and Summers P. W.: The vertical transport and redistribution of pollutants by clouds, in: Specialty Conf. on the Meteorology of Acid Deposition, October 1983, edited by: Samson, P. J., Pittsburg, PA: Air Pollution Control Association, 496–512, 1983.

Jacob, D. J.:Introduction to Atmospheric Chemistry. Princeton, New Jersey: Princeton University Press, 1999.

Kiley, C. M. and Fuelberg, H. E.: An examination of summertime cyclone transport processes during Intercontinental Chemical Transport Experiment (INTEX-A), J. Geophys. Res., 111, D24S06, doi:10.1029/2006JD007115, 2006.

Klemp, J. B. and Wilhelmson, R. B.: The simulation of three-dimensional convective storm dynamics, J. Atmos. Sci., 35, 1070–1096, 1978.

Kulawik S. S., Worden, H., Osterman, G., Luo, M., Beer, R., Kinnison, D. E., Bowman, K. W., Worden, J., Eldering, A., Lampel, M., Steck, T., and Rodgers, C. D.: TES atmospheric profile retrieval characterization: An orbit of simulated observations, IEEE Trans. Geosci. Rem. Sens., 44, 1324–1333, 2006.

Kulawik, S.S. Personal communication. 7 March 2007.

Lericos, T. P., Fuelberg, H. E., Weisman, M. L., and Watson A. I.: Numerical simulations of the effects of coastlines on the evolution of strong, long-lived squall lines, Mon. Weaher Rev., 135, 1710–1731, 2006.

Lin, Y.-L., Farley, R. D., and Orville, H. D.: Bulk parameterization of the snow field in a cloud model, J. Appl. Meteor., 22, 1065–1092, 1983.

Luo, M., Beer, R., Jacob, D. J., Logan, J. A., and Rodgers, C. D.: Simulated observation of tropospheric ozone and CO with the Tropospheric Emission Spectrometer (TES) satellite instrument, J. Geophys. Res., 107(D15), 4270, doi:10.1029/2001JD000804, 2002,

Luo, M., Rinsland, C. P., Rodgers, C. D., Logan, J. A., Worden, H., Kulawik, S., Eldering, A., Goldman, A., Shephard, M. W., Gunson, M., and Lampel, M.: Comparison of carbon monoxide measurements by TES and MOPITT: Influence of a priori data and instrument characteristics on nadir atmospheric species retrievals, J. Geophys. Res., 112, D09303, doi:10.1029/2006JD007663, 2007.

Luo, M., Worden, H., and TES team: Steps of making comparisons of TES nadir retrievals to

your profiles with higher vertical resolution, http://tes.jpl.nasa.gov/temp/Web_help/web.html, 2007.
NASA Facts On Line: Measurement of Air Pollution from Satellites (MAPS) – understanding the chemistry of the atmosphere, 19 September 1996, http://oea.larc.nasa.gov/PAIS/MAPS.html, 2007.
Niewiadomski, M.: A passive pollutant in a three-dimensional field of convective clouds: Numerical simulations, Atmos. Environ., 20, 139–145, 1986.
Ogura, Y. and Liou, M.: The structure of a midlatitude squall line: A case study, J. Atmos. Sci., 37, 553–567, 1980.
Park, R. J., Stenchikov, G. L., Pickering, K. E., Dickerson, R. R., Allen, D. J., and Kondragunta, S.: Regional air pollution and its radiative forcing: Studies with a single-column chemical and radiation transport model, J. Geophys. Res., 106, 28 751–28 770, 2001.
Pickering, K. E., Dickerson, R. R., Luke, W. T., and Nunermacker, L. J.: Clear sky vertical profiles of trace gases as influenced by upstream convective activity, J. Geophys. Res., 94, 14 879–14 892, 1989.
Pickering, K. E., Thompson, A. M., Dickerson, R. R., Luke, W. T., McNamara, D. P., Greenberg, J. P., and Zimmerman, P. R.: Model calculations of tropospheric ozone production potential following observed convective events, J. Geophys. Res., 95, 14 049–14 062, 1990.
Pickering, J. E., Thompson, A. M., Scala, J. R., Tao, W.-K., Simpson, J., and Garstang, M.: Photochemical ozone production in tropical squall line convection during NASA/GTE/ABLE 2A, J. Geophys. Res., 96, 3099–3114, 1991.
Pickering, J. E., Thompson, A. M., Scala, J. R., Tao, W.-K., and Simpson, J.: Ozone production potential following convective redistribution of biomass emissions, J. Atmos. Chem., 14, 297–313, 1992a.
Pickering, J. E., Scala, J., Thompson, A. M., Tao, W.-K., and Simpson, J.: A regional estimate of convective transport of CO from biomass burning, Geophys. Res. Lett., 19, 289–292, 1992b.
Pickering J. E., Thompson, A. M., Scala, J. R., Tao, W.-K., Dickerson, R. R., and Simpson, J.: Free tropospheric ozone production following entrainment of urban plumes into deep convection, J. Geophys. Res., 97, 17 985–18 000, 1992c.
Pickering, J. E., Thompson, A. M., Tao, W., Rood, R. B., McNamara, D. P., and Molod, A. M.: Vertical transport by convective clouds: Comparisons of three modeling approaches, Geophys. Res. Lett., 22, 1089–1092, 1995.
Rodgers, C. D.: Inverse Methods for Atmospheric Sounding, Theory and Practice, Hackensack,

ACPD
8, 19201–19247, 2008

New Jersey: World Scientific Publishing Co., 2000.
Rodgers, C. D. and Connor, B. J.: Intercomparison of remote sounding instruments, J. Geophys. Res., 108(D3), 4116, doi:10.1029/2002JD002299, 2003.
Rotunno, R., Klemp, J. B., Weisman, M. L.: A theory for strong, long-lived squall lines, J. Atmos. Sci., 45, 463–485, 1987.
Scala, J., Garstang, M., Tao, W.-K., Pickering, K., Thompson, A., Simpson, J., Kirchhoff, V., Browell, E., Sachse, G., Torres, A., Gregory, G., Rasmussen, R., and Khalil, M.: Cloud draft structure and trace gas transport, J. Geophys. Res., 95, 17 015–17 030, 1990.
Singh, H. B., Brune, W. H., Crawford, J. H., Jacob, D. J., and Russell, P. B.: Overview of the summer 2004 Intercontinental Chemical Transport Experiment–North America (INTEX-A), J. Geophys. Res., 111, D24S01, doi:10.1029/2006JD007905, 2006.
Singh, H. B., Brune, W. H., Crawford, J. H., Fuelberg, H. E., and Jacob, D. J., et al.: Chemistry and transport of pollution over the Gulf of Mexico and the Pacific: Spring 2006 INTEX-B campaign overview and first results, Atmos. Chem and Phys. Discuss., accepted, 2008.
Soong, S.-T. and Ogura, Y.: Response of trade wind cumuli to large-scale processes: J. Atmos. Sci., 37, 2035–2050, 1980.
Soong, S.-T. and Tao, W.-K.: Response of deep tropical clouds to mesoscale processes, J. Atmos. Sci., 37, 2016–2036, 1980.
Stenchikov, G., Dickerson, R., Pickering, K., Ellis, W., Doddridge, B., Kondragunta, S., Poulida, O., Scala, J., Tao, W.-K.: Stratosphere-troposphere exchange in a mid-latitude mesoscale convective complex: Part 2, Numerical simulations, J. Geophys. Res., 101, 6837–6851, 1996.
Tao, W.-K. and Simpson, J.: Cloud interactions and merging: Numerical simulations, J. Atmos. Sci., 41, 2901–2917, 1984.
Tao, W.-K. and Simpson, J.: Goddard cumulus ensemble model. Part 1: Model description, Terr. Atmos. Oceanic Sci., 4, 35–72, 1993.
Tao, W.-K., Simpson, J., Baker, D., Braun, S., Chou, M.-D., Ferrier, B., Johnson, D., Khain, A., Lang, S., Lynn, B., Shie, C.-L., Starr, D., Sui, C.-H., Wang, Y., and Wetzel, P.: Microphysics, radiation and surface processes in the Goddard Cumulus Ensemble (GCE) model, Meteorol. Atmos. Phys., 82, 97–137, 2003.
Tao, W.-K., Simpson, J., and Soong, S.-T.: Numerical simulation of a subtropical squall line over the Taiwan Strait, Mon. Weather Rev., 119, 2699–2723, 1991.
Tao, W.-K. and Soong, S.-T.: A study of the response of deep tropical clouds to mesoscale

processes: Three-dimensional model experiments, J. Atmos. Sci., 43, 2653–2676, 1986.
Osterman, G.: TES L2 Data User's Guide. Vers. 1.00. 11 Apr. 2006. Jet Propulsion Laboratory, California Institute of Technology, http://tes.jpl.nasa.gov/docsLinks/DOCUMENTS/TESL2DataUsersGuidev2.0.pdf, 2006.
Thompson, A. M., Pickering, K. E., Dickerson, R. R., Ellis Jr., W. G., Jacob, D. J., Scala, J. R., Tao, W.-K., McNamara, D. P., and Simpson, J.: Convective transport over the central United States and its role in regional CO and ozone budgets, J. Geophys. Res., 99, 18 703–18 712, 1994.
Thompson, A. M., Tao, W. K., Pickering, K. E., Scala, J. R., and Simpson, J.: Tropical deep convection and ozone formation, Bull. Amer. Meteor. Soc., 78, 1043–1054, 1997.
Thorpe, A. J., Miller, M. J., and Moncrieff, M. W.: Two-dimensional convection in non-constant shear: a model of mid-latitude squall lines, Quart. J. R. Met. Soc.,108, 739–762, 1982.
Tremblay, A. and Leighton, H.: A three-dimensional cloud chemistry model, J. Clim. Appl. Meteorol., 25, 652–671, 1986.
Wang, Y., Jacob, D. J., and Logan, J. A.: Global simulation of tropospheric O3-NOx-hydrocarbon chemistry: 1. Model formulation, J. Geophys. Res., 103, 10 713–10 725, 1998a.
Warning Decision Support System – Integrated Information. NOAA/National Severe Storms Laboratory, University of Oklahoma, http://www.wdssii.org/, 2007.
Weisman, M. L. and Klemp, J. B.: The dependence of numerically simulated convective storms on wind shear and buoyancy, Mon. Weather Rev., 110, 504–520, 1982.
Weisman, M. L. and Klemp, J. B.: The structure and classification of numerically simulated con-vective storms in directionally varying wind shear, Mon. Weather Rev., 112, 2479–2498, 1984.
Weisman, M. L., Klemp, J. B., and Rotunno, R.: Structure and evolution of numerically simulated squall lines, J. Atmos. Sci., 45, 1990–2013, 1988.
Weisman, M. L. and Rotunno, R.: A theory for strong long-lived squall lines revisited, J. Atmos. Sci., 61, 361–382, 2004.
Zhang, G. J. and McFarlane, N. A.: Sensitivity of climate simulations to the parameterization of cumulus convection in the Canadian Climate Centre general circulation model, Atmos. Ocean, 33, 407–446, 1995.

Table 1. GCE model domain and parameter settings used in this study.

Parameter	Configuration
Physical domain (x-z)	514 km×25 km
Horizontal grid spacing (stretched)	
Min	750 m
Max	1000 m
Vertical grid spacing (stretched)	
Min	220 m
Max	1050 m
Calculation time step	2 s
Coordinate system velocity	0 m s^{-1}
Uniform initial conditions	TRUE
Cold pool parameters	
Width	8 km
Depth	1.5 km
Cooling rate	7.0×10^{-3} K s^{-1}
Boundary conditions	
Top	5 km Rayleigh relaxation (absorbing) layer
Bottom	Free-slip
Lateral	Open (Klemp and Wilhelmson, 1978)
Microphysics	
Liquid water	Kessler-type (Cloud water and rain)
Ice	Three-category (Cloud ice, snow, graupel) Lin et al. (1983)

ACPD
8, 19201–19247, 2008

Table 2. CO vertical mass flux (metric tons per 10 min) for the entire 8 h simulation period.

Pressure level and calculation	
Upward mass flux (metric tons)	
300 hPa	96.0
500 hPa	129.5
850 hPa	33.0
Downward mass flux (metric tons)	
300 hPa	67.1
500 hPa	101.9
850 hPa	45.6
Net mass flux (metric tons)	
300 hPa	28.9
500 hPa	27.6
850 hPa	–12.6

ACPD
8, 19201–19247, 2008

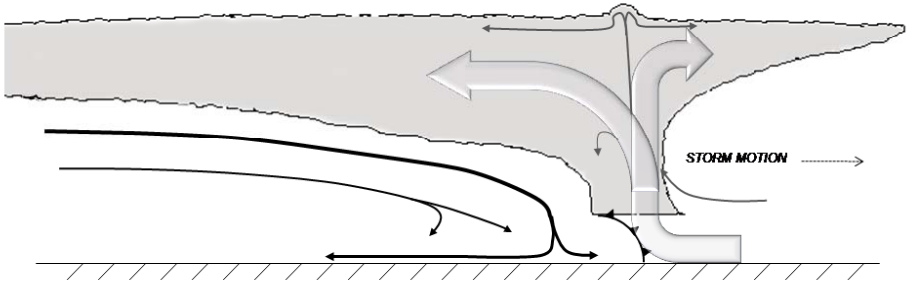

Fig. 1. Schematic of the flow regimes in a mesoscale convective system (adapted from Houze et al., 1989). Large hollow arrows identify the ascending front to rear inflow (left) and core updraft transporting air to the cloud top and forward anvil (right). Black arrows represent the rear inflow jet supporting the cold pool generation directly below the core updraft.

ACPD

8, 19201–19247, 2008

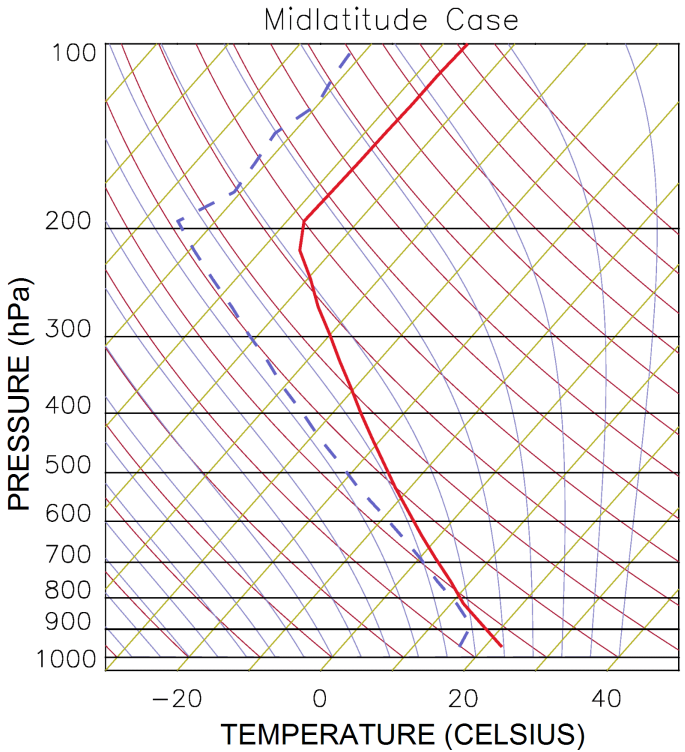

Fig. 2. Thermodynamic sounding of the pre-squall line environment used for the squall line simulation in this study. The solid red line denotes temperature, while the dashed blue line shows dew point temperature.The sounding is similar to that at Lincoln, IL at 00:00 UTC 13 March 2006.

ACPD
8, 19201–19247, 2008

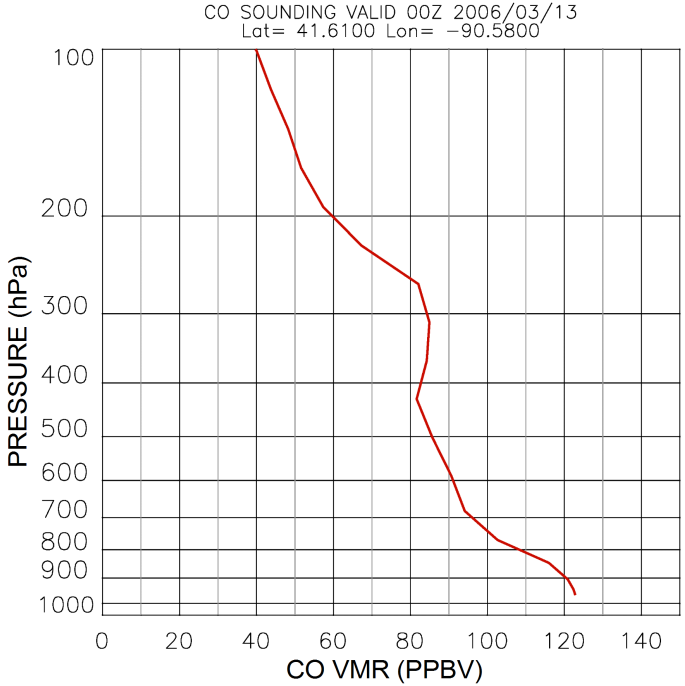

Fig. 3. CO profile (ppbv) from the GEOS-Chem model used as the background concentration in the GCE for the squall line simulation. The profile is valid at 00:00 UTC 13 March 2006 at 41.61° N, 90.58° W.

ACPD
8, 19201–19247, 2008

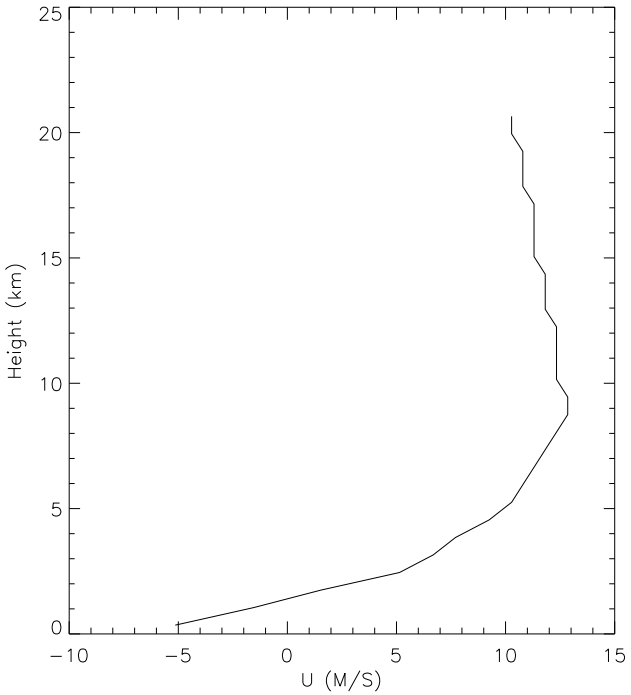

Fig. 4. The vertical wind profile used in the squall line simulation.

ACPD
8, 19201–19247, 2008

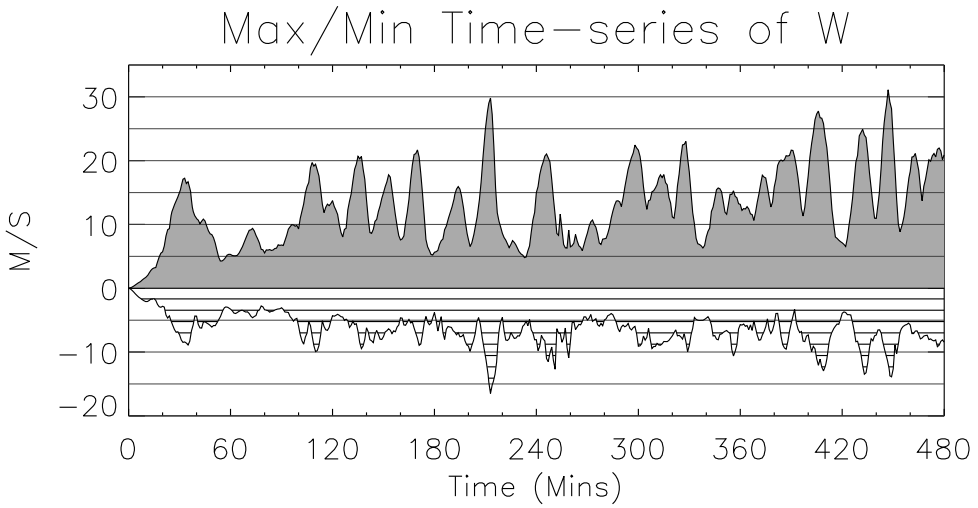

Fig. 5. Time-series of maximum updraft speed (positive values) and maximum downdraft speed (negative values) in $m\,s^{-1}$ during the entire 8-h squall line simulation period.

ACPD
8, 19201–19247, 2008

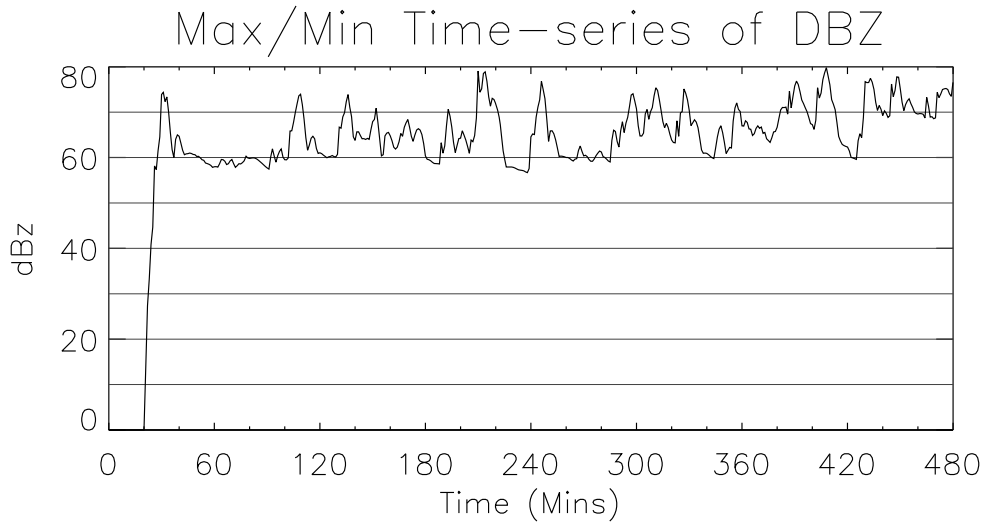

Fig. 6. Time-series of maximum model simulated radar reflectivity (dBZ) during the squall line simulation period.

ACPD
8, 19201–19247, 2008

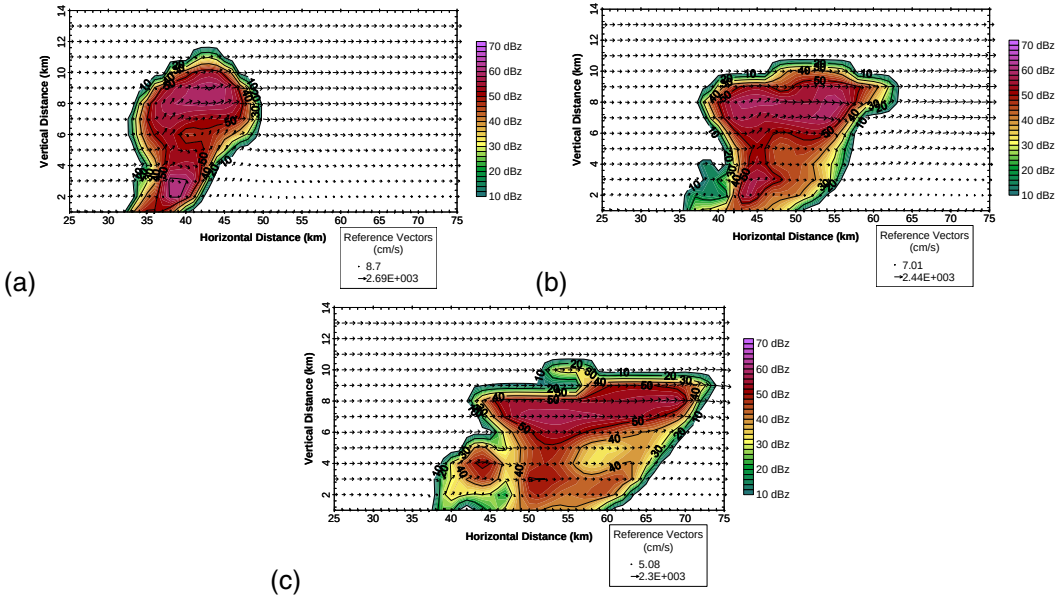

Fig. 7. U-W wind vectors and reflectivities (dBZ) at **(a)** 40 min, **(b)** 50 min, and **(c)** 60 min into the simulation. The longest arrow represents the maximum wind of (a) 27 m s^{-1}, (b) 24 m s^{-1}, and (c) 23 m s^{-1}.

ACPD
8, 19201–19247, 2008

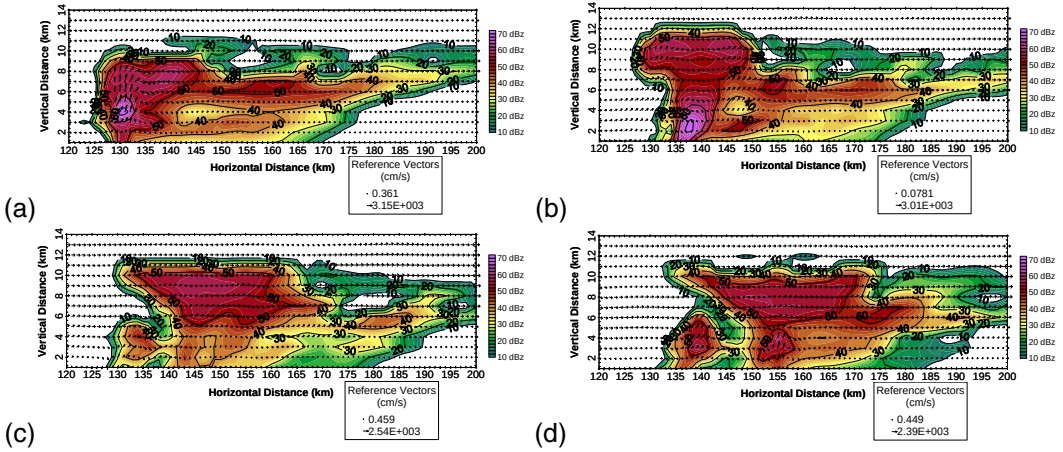

Fig. 8. Time series of U-W wind vectors and reflectivity (dBZ) at 10 min intervals from **(a)** 210 min to **(d)** 240 min into the simulation. The domain is centered on the region of reflectivity at the time. The longest arrow represents 31 m s^{-1} wind speeds in (a), decreasing to 24 m s^{-1} in (d).

ACPD
8, 19201–19247, 2008

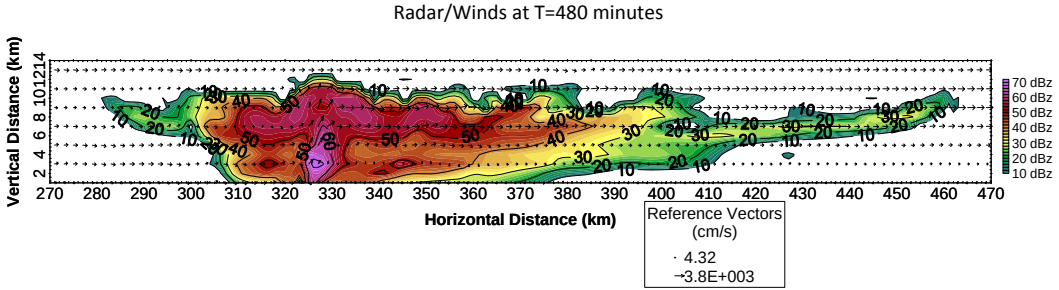

Fig. 9. Reflectivity pattern (dBZ) at the end of the 8 h simulation.

ACPD
8, 19201–19247, 2008

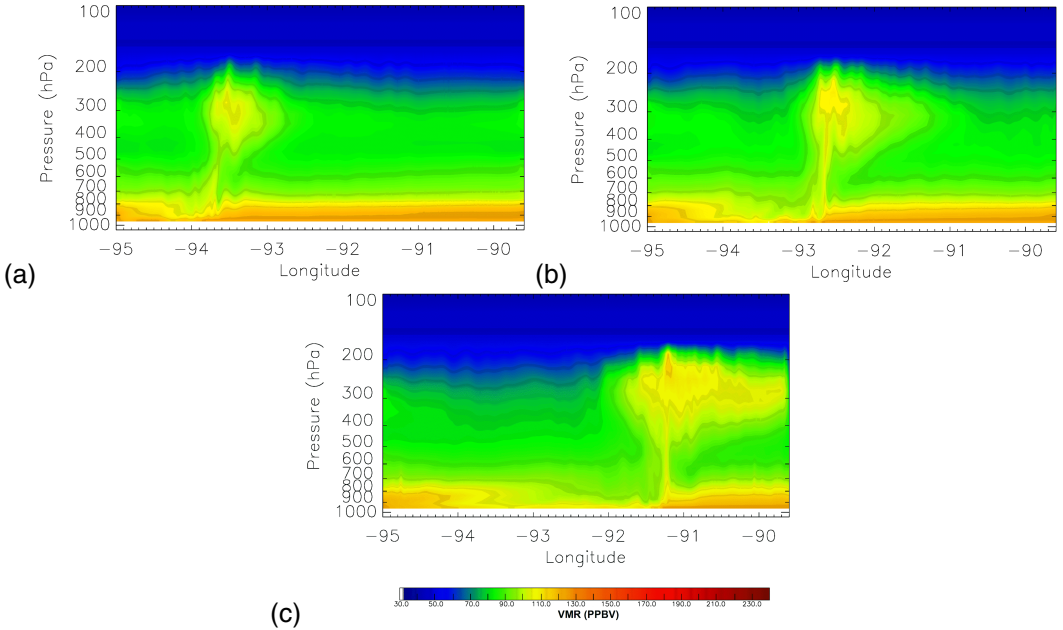

Fig. 10. CO concentration (ppb) for the model domain after **(a)** 180 min, **(b)** 310 min, and **(c)** 480 min.

ACPD
8, 19201–19247, 2008

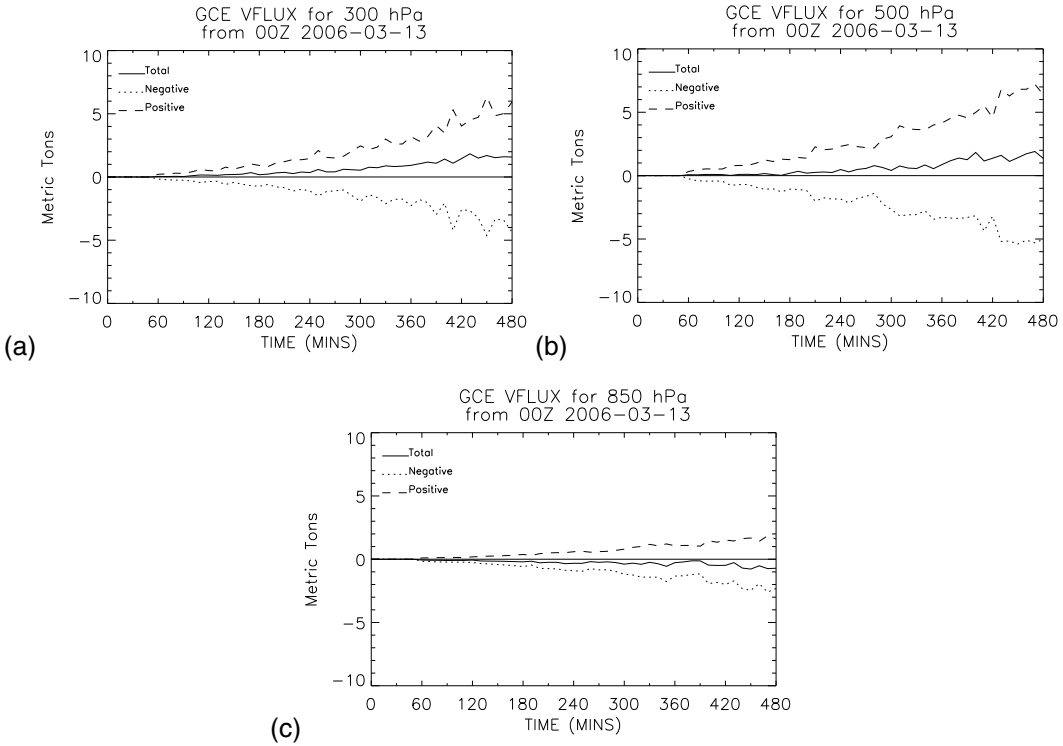

Fig. 11. Time series of vertical CO mass flux (metric tons per 10 min period) at **(a)** 300 hPa **(b)** 500 hPa, and **(c)** 850 hPa during the entire model simulation period.

ACPD
8, 19201–19247, 2008

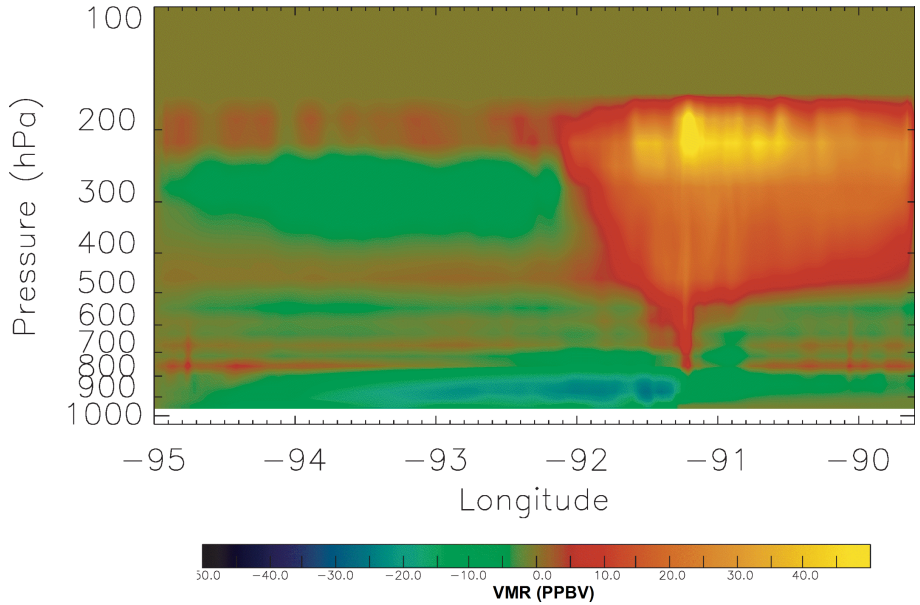

Fig. 12. Change in CO concentration over the total model domain (ppbv) during the overall 8 h simulation.

ACPD
8, 19201–19247, 2008

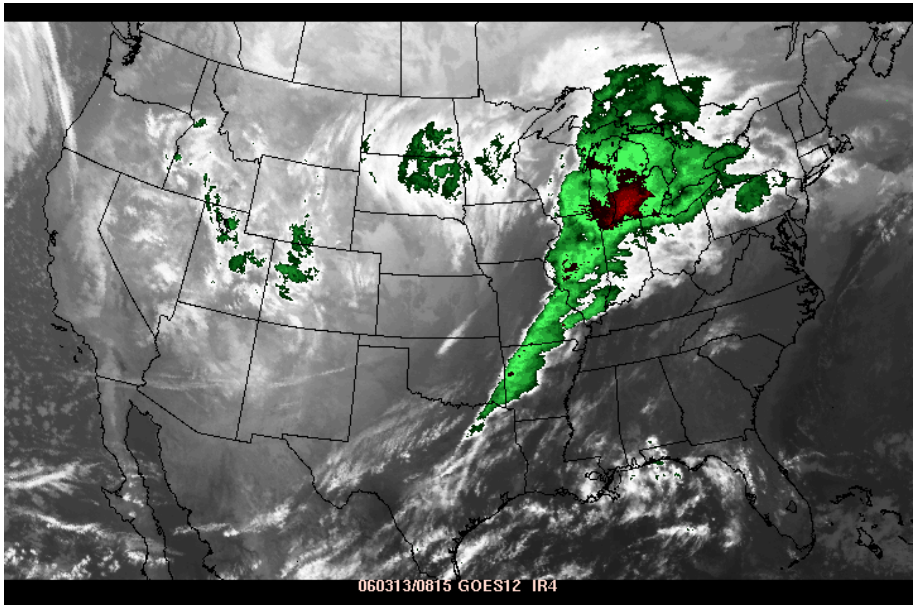

Fig. 13. GOES-12 enhanced infrared satellite image for 08:15 UTC 13 March 2006.

ACPD

8, 19201–19247, 2008

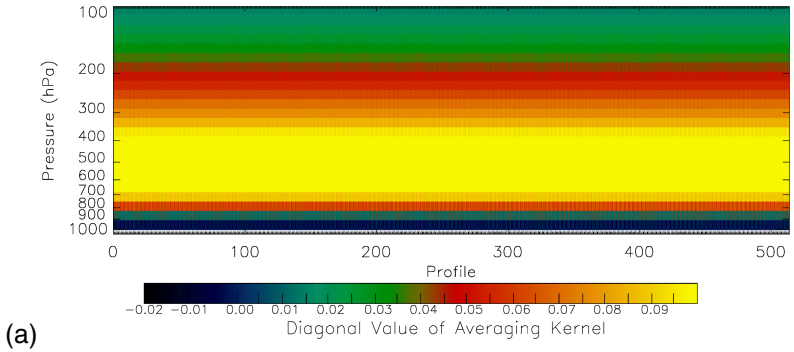

(a)

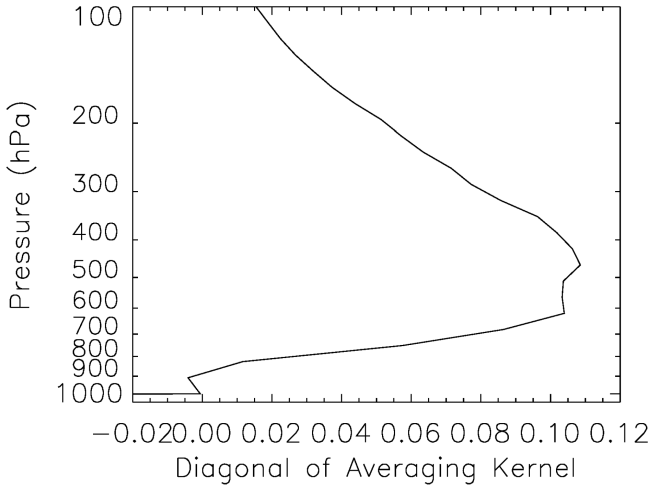

(b)

Fig. 14. (a) Clear sky averaging kernel diagonal used in the TES retrievals from profile 17 of RUNID 3443 on 13 March 2006 that was applied to all horizontal grid points in the 2-D GCE model domain **(b)** Averaging kernel diagonal profile for an individual location.

ACPD
8, 19201–19247, 2008

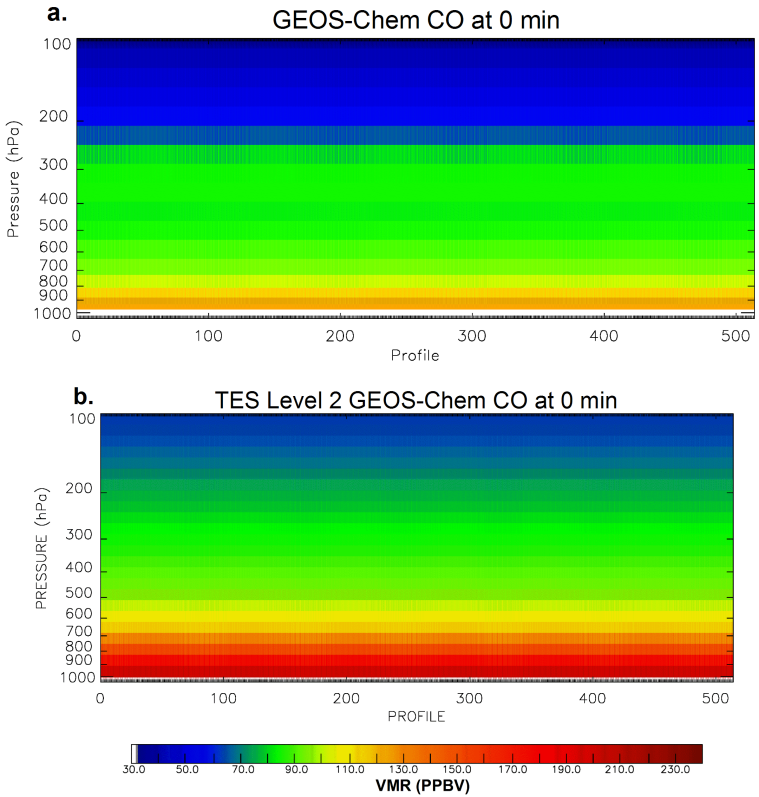

Fig. 15. **(a)** Initial CO concentration (ppbv) used in the GCE simulation, **(b)** Synthetic TES retrievals of the initial CO concentration (ppbv).

ACPD
8, 19201–19247, 2008

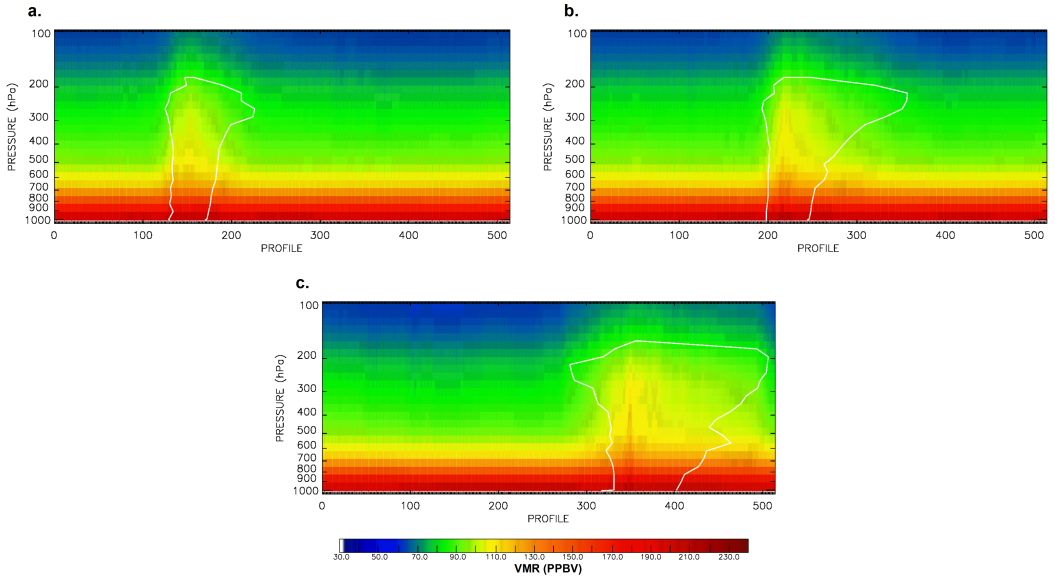

Fig. 16. Synthetic TES retrievals (ppbv) for the GCE model domain at **(a)** 180 min, **(b)** 300 min, and **(c)** 480 min. The white outline in the figure is the region of clouds associated with the storm system. TES retrievals in regions below and within this area are interpereted as being unrealible because of the "clear-sky" averaging kernel used for the profiles.

ACPD
8, 19201–19247, 2008

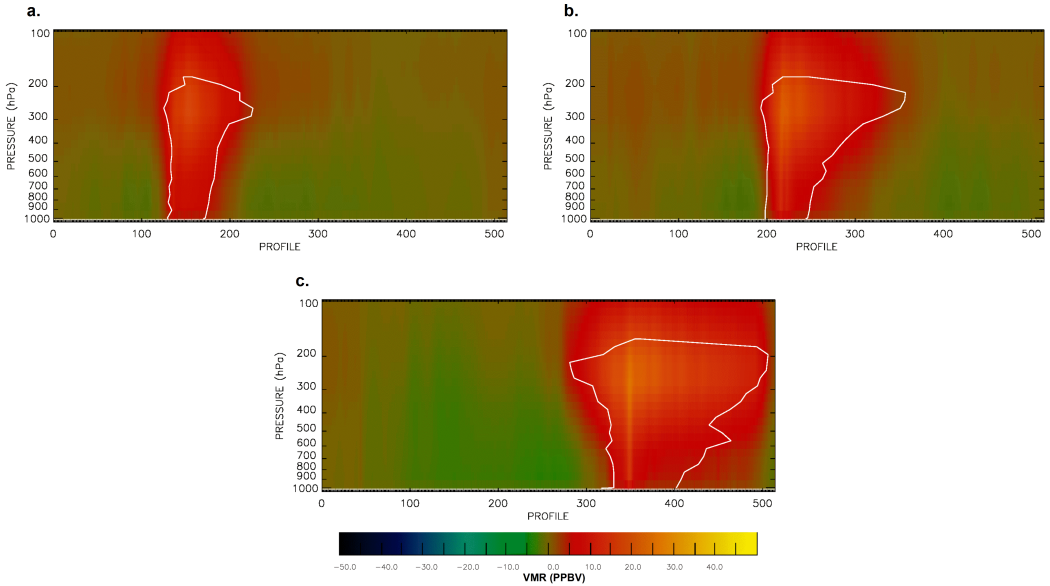

Fig. 17. Plots of the difference (ppbv) between synthetic TES CO retrievals and the initial CO concentration (as seen by TES) at **(a)** 180 min, **(b)** 300 min, and **(c)** 480 min. The white outline is the region of the storm's clouds, as in Fig. 16.

ACPD
8, 19201–19247, 2008

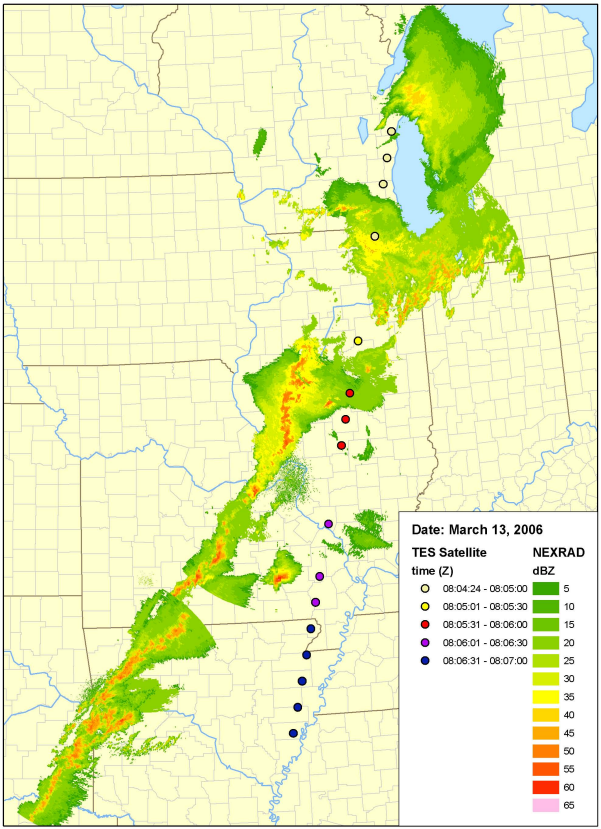

Fig. 18. Radar reflectivity of the squall line (dBZ) at 08:04 UTC 13 March 2006, along with TES retrieval locations. TES moves from NE (location 0) to SW (location 15), crossing the squall line near Lincoln, IL. The TES footprints are color-coded to show the time of each retrieval.

ACPD
8, 19201–19247, 2008

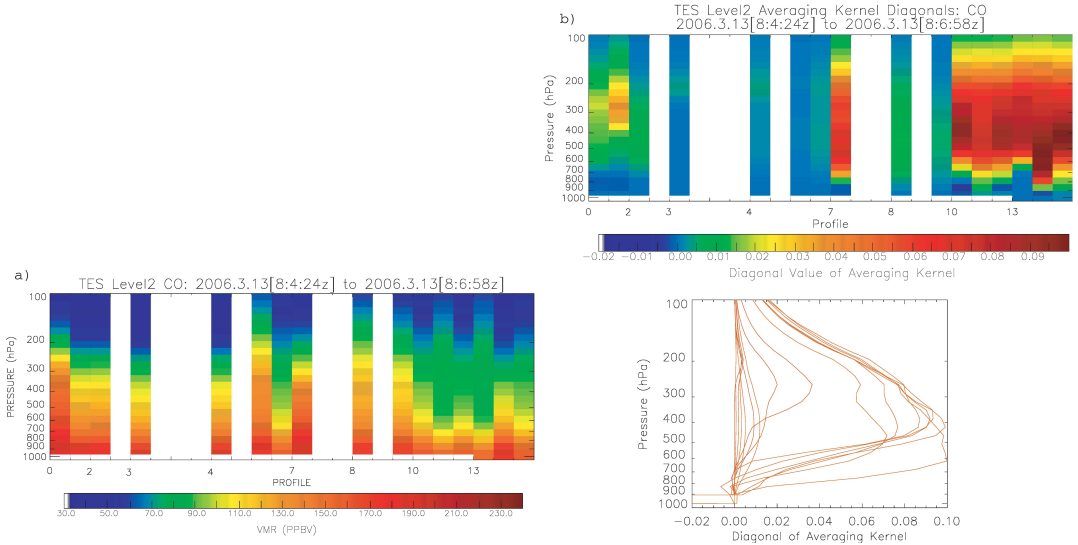

Fig. 19. (a) TES CO retrievals (ppbv) for RUNID 3443 at 08:04 UTC 13 March 2006 for profiles 0–15, **(b)** TES averaging kernel diagonals for RUNID 3443 and profiles 0–15.

ACPD
8, 19201–19247, 2008